Journal of Cleaner Production 566 (2026) 148565

Contents lists available at ScienceDirect

Journal of Cleaner Production

journal homepage: www.elsevier.com/locate/jclepro

Theoretical model development and performance analysis of magnetic heat-assisted multi-stage solar stills for water production

Chenghua Zhang [a], Yunfei Yan [a,*], Yonghong Wu [a], Zikang Niu [a], Wen Siang Lew [b,**]

[a] Key Laboratory of Low-grade Energy Utilization Technologies and Systems, Chongqing University, Ministry of Education, Chongqing, 400030, China
[b] School of Physical and Mathematical Sciences, Nanyang Technological University, 21 Nanyang Link, Singapore, 637371

HIGHLIGHTS

- Dual-input solar still enables tunable water production up to 9.92 kg m^{-2} h^{-1}.
- Front-loaded evaporation and stage limits are identified with dissipation penalties.
- Optimization covers chamber height, radius, thickness, and magnetothermal input.
- At 2130 W m^{-2}, η_{tot} reaches 335.29% via excellent multi-stage energy recovery.

ARTICLE INFO

Keywords:
Multi-stage solar stills
Magnetic heat-assisted
Theoretical model
Evaporation performance
Energy efficiency

ABSTRACT

Multi-stage solar stills improve energy efficiency by recycling condensation latent heat; however, conventional designs are limited by fluctuating solar irradiation and boundary heat losses, resulting in a restricted effective stage number and performance saturation. Here, we propose a photothermal-magnetothermal dual-input magnetic heat-assisted multi-stage solar still (MHMSS), in which a magnetic porous carbon film acts as an integrated energy-conversion layer, generating heat under both solar irradiation and an alternating magnetic field. A comprehensive multi-stage heat and mass transfer model is developed to predict and optimize distillation performance, showing good agreement with experiments, with relative deviations of 3.77%-5.14% for evaporation rate and 2.10%-4.29% for glass-sheet outlet temperature. The system exhibits upstream-dominated water production with diminishing returns as the stage number increases, while heat dissipation through the top wall and sidewalls primarily limits the effective working stages. Parametric analysis indicates that reducing the chamber height H enhances latent heat recovery, although excessively small gaps risk condensate contamination; an optimal H of 0.4 cm is recommended by balancing efficiency and water quality. Increasing the evaporation-surface radius R and sidewall thickness t further suppresses heat losses, and the phase-change driving force can be substantially strengthened by regulating the magnetothermal input. At a total input power of 2130 W m^{-2}, the total efficiency (η_{tot}) and recoverable efficiency (η_{rec}) reach 335.29% and 283.82%, respectively, with an evaporation rate of 10.91 kg m^{-2} h^{-1}. This research demonstrates the synergistic coupling of regulated magnetothermal heating with multi-stage latent heat cascading, supported by a unified theoretical framework that quantitatively elucidates the effects of stage configuration, structural optimization, and operating conditions, providing theoretical insight into the design of high-performance multi-stage solar stills for water production.

1. Introduction

In recent years, escalating global water-security risks have made a secure, reliable, and sustainable freshwater supply a critical constraint on socioeconomic development (Yuan et al., 2025; Miao et al., 2023; Chang et al., 2024). According to the United Nations World Water Development Report 2024, approximately half of the global population experiences severe water scarcity, with nearly one quarter living under extremely high water stress (UN-Water, 2024). Given that oceans cover 71% of the Earth's surface, seawater represents the most abundant

* Corresponding author.
** Corresponding author.
E-mail addresses: yunfeiyan@cqu.edu.cn (Y. Yan), wensiang@ntu.edu.sg (W.S. Lew).

https://doi.org/10.1016/j.jclepro.2026.148565
Received 2 March 2026; Received in revised form 23 April 2026; Accepted 17 May 2026

unconventional water resource, making desalination a promising pathway for freshwater production (Li et al., 2024). Currently, large-scale desalination is dominated by thermal processes (multi-stage flash, MSF; multi-effect distillation, MED) and membrane-based technologies (reverse osmosis, RO) (Liu et al., 2025; Yu and Wang, 2022; Liu et al., 2024). Despite widespread commercialization, these systems are often constrained by high-grade energy demands, substantial infrastructure requirements, and site-specific limitations associated with coastal deployment (Xiao et al., 2025; Yang et al., 2023; Cui et al., 2025). Consequently, the development of renewable energy driven, low-carbon, off-grid, and portable desalination technologies suitable for offshore islands, marine vessels, and deep-sea platforms is of significant scientific and practical interest.

Solar-driven seawater desalination has attracted sustained attention due to the abundance of solar energy and its compatibility with off-grid and distributed deployment (Zhang et al., 2025; Yang et al., 2022). Conventional solar distillation relies on bulk heating of seawater to induce evaporation and condensation (Li et al., 2021), but severe heat losses through bulk conduction, device-wall dissipation, and convective-radiative transfer limit energy utilization and constrains areal water yield (Fujiwara and Kikuchi, 2017). To address these limitations, solar-driven interfacial evaporation has rapidly advanced by localizing photothermal heating at the air-water interface, enabling higher interfacial temperatures and evaporation driving forces without significantly heating the bulk water, thereby suppressing heat loss and improving solar to vapor conversion efficiency (Lu et al., 2025; S. Liu et al., 2023). Interfacial evaporator design focuses on efficient solar absorption and photothermal conversion (Tian et al., 2025), continuous capillary water supply (Zhang et al., 2025), and effective thermal management (Cheng et al., 2025). A diverse range of photothermal materials, including carbon-based materials (Zhou et al., 2021), organic absorbers (Ma et al., 2025), semiconductors (Liu et al., 2023), metal nanoparticles (Jiang et al., 2025), and emerging two-dimensional materials, have been explored and further optimized through composite engineering and interfacial tailoring to achieve high solar absorptance (Yu et al., 2023). In parallel, supporting architectures such as porous aerogels, fibrous membranes, biomimetic wood channels, and hydrogel networks have been developed to enable rapid water transport and vapor escape while maintaining heat localization via low effective thermal conductivity (Zhang et al., 2024; Li et al., 2022; Yu et al., 2024; Ma et al., 2021). Under one sun irradiation (1000 W m^{-2}), interfacial evaporation fluxes typically reach 1–2 kg m^{-2} h^{-1}, significantly exceeding that of bulk water evaporation (~0.37 kg m^{-2} h^{-1}) (Wu et al., 2022), with advanced designs incorporating enhanced thermal management, optical trapping, or reduced apparent evaporation enthalpy achieving rates above 4 kg m^{-2} h^{-1} (Yang et al., 2022). Nevertheless, the intermittency and variability of solar irradiation have motivated increasing efforts to integrate supplementary energy inputs, such as industrial waste heat (Luo et al., 2024), wave energy (Deng et al., 2022), electrothermal heating (Fang et al., 2024), and magnetothermal conversion (Zhang et al., 2026), to further enhance interfacial evaporation and enable continuous freshwater production, offering a promising strategy for next-generation solar desalination systems.

Although solar interfacial evaporation can achieve high evaporation rates, the latent heat released during vapor condensation is generally not recovered and is instead dissipated to the surroundings as waste heat. This single-stage heat utilization fundamentally constrains overall energy efficiency and limits further gains in areal freshwater yield (Tian et al., 2024). To overcome this limitation, multistage stills have been proposed to enable latent-heat recovery and cascade reuse by arranging evaporation-condensation units in series. In such architectures, vapor generated in an upstream stage condenses in a downstream stage, releasing heat that simultaneously drives evaporation of the downstream interfacial water film, thereby enabling repeated utilization of condensation latent heat (Wang et al., 2022; Chiavazzo et al., 2018; Liu et al., 2024). Notably, when auxiliary energy inputs, such as electrothermal heating, magnetothermal conversion, or waste heat, are introduced to enhance evaporation flux and enable continuous water production, the rate of latent-heat release increases accordingly (Shi et al., 2023). Compared with other auxiliary energy sources, magnetothermal assistance is characterized by non-contact energy input, localized heating within the functional layer, and good tunability of the supplementary heat source, making it particularly suitable for coupling with solar interfacial evaporation under fluctuating irradiation conditions (Du et al., 2025). However, in the absence of matched condensation modules and efficient heat-recovery configurations, latent-heat losses are further amplified, underscoring the necessity of multistage evaporation–condensation architectures (Zhang et al., 2024). Despite recent advances in heat and mass transfer modeling and parametric sensitivity analyses for multistage systems, more systematic mechanistic modeling and experimental validation remain essential to quantitatively elucidate the coupled relationships among energy utilization, vapor transport, condensation yield, and interfacial evaporation, and to establish transferable design guidelines for structural optimization and scale-up (Luo et al., 2024; Zhang et al., 2025).

In this work, we target system-level enhancement of solar interfacial evaporation assisted by magnetothermal heating. We develop a multistage distillation architecture featuring dual energy inputs from photothermal and magnetothermal sources, and propose a theoretical framework tailored for capillary-fed multistage systems to quantitatively predict interstage temperature distributions, evaporation rates, and energy efficiency. The model is calibrated and validated against key experimental measurements, establishing a reliable predictive methodology. On this basis, we conduct a comparative analysis of coupled heat and mass transfer in single-stage and multistage stills, systematically elucidating the conductive, convective, and radiative heat-loss pathways that constrain efficiency improvement. Through parametric analysis of key design parameters, we further reveal performance dependence on geometric parameters, including chamber height H, evaporating-surface radius R, and sidewall thickness t, and evaluate the coupled effects of magnetothermal input power and ambient conditions on evaporation driving force and cascaded latent-heat recovery. Collectively, this study establishes a quantitative design and performance-prediction framework for multistage interfacial evaporation systems, providing a theoretical basis for the structural design and operational control of efficient and scalable solar desalination devices.

2. Working principle and theoretical analysis

The magnetic heat-assisted multi-stage solar still (MHMSS) is designed to efficiently utilize solar and magnetothermal energy for vapor generation, while maximizing the recovery of the evaporation heat and minimizing heat losses. This section describes the working principle of the MHMSS, the construction of the physical model, and the development of the theoretical model.

2.1. Working principle

As illustrated in Fig. 1, the MHMSS integrates a top absorber layer, multiple stacked evaporation-condensation stages, thermally insulated side walls, and a bottom heat-dissipation module to enable cascade heat recovery. During operation, seawater is continuously supplied from the feed tank and delivered into each evaporation stage through a superhydrophilic wicking layer, where a thin saline film is maintained to promote interfacial evaporation. Under solar irradiation, the absorber layer converts incident light into localized heat, rapidly increasing the temperature of the upper evaporation interface. Simultaneously, when an alternating magnetic field (AMF) is applied, the magnetothermal component provides an additional, controllable heat input by magnetothermal effect. The combined photothermal–magnetothermal heating enhances vapor generation and stabilizes the power input under weak or fluctuating sunlight, and the generated vapor migrates to the adjacent

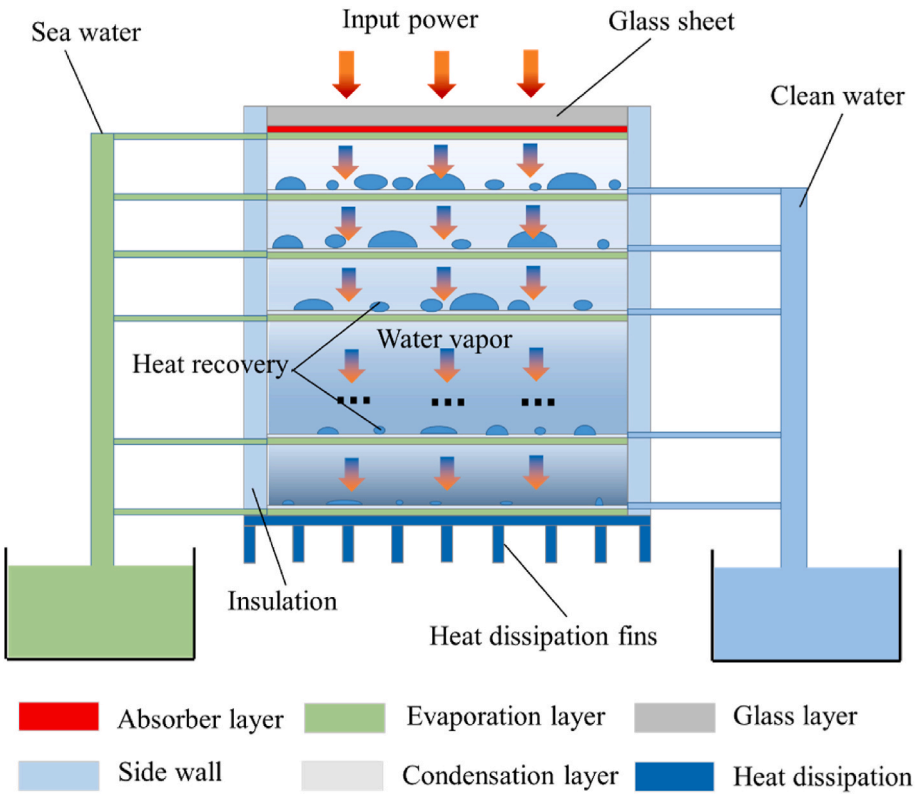

Fig. 1. Schematic design of the magnetic heat-assisted multi-stage solar still (MHMSS). Seawater (left) is delivered into the MHMSS through a superhydrophilic wicking layer, and freshwater is produced via multistage evaporation–condensation and subsequently transported by the wicking layer to the freshwater reservoir (right) for collection.

cooler condensation layer and condenses into liquid water droplets. Importantly, the released latent heat of condensation and sensible heat transfer is transferred downward to the next evaporation stage, driving subsequent evaporation. This multistage evaporation-condensation cascade enables repeated utilization of the input heat across stages, thereby improving the effective energy efficiency and freshwater yield compared with a single-stage still. To sustain a strong driving force for condensation and directional vapor transport, the bottom fins continuously remove residual heat and maintain a favorable axial temperature gradient. Meanwhile, the insulated side walls suppress parasitic heat losses and vapor loss, the condensed freshwater is collected and guided to the clean-water reservoir, whereas the remaining brine becomes concentrated in the evaporation layers and can be discharged or recirculated.

2.2. Physical model and experimental system

As shown in Fig. 2, the physical model, assembly configuration, and experimental platform of the MHMSS are presented (Figs. S1 and S2). In Fig. 2a, the MHMSS physical model mainly consists of three parts: a top cover for fixing the glass sheet, repeated multistage distillation units for the evaporation–condensation process, and a finned base for enhanced heat dissipation to maintain a relatively low temperature. All components are designed with alignment features for reliable assembly and are globally tightened and sealed using a bolt–nut set, thereby ensuring stable inter-stage distance and structural integrity. This modular architecture enables convenient adjustment of the stage number by adding or removing unit modules, providing a structural basis for performance comparison and theoretical modeling. Furthermore, as shown in Fig. 2b, the MHMSS components were fabricated by the PC-based 3D-printed (left). A superhydrophilic water ripple paper was employed as the wicking layer, and an ultrathin plastic film was used as the condensation layer. Both the wick and the condensation film were fixed within each repeated unit, and an outlet channel was reserved to guide and collect the condensed freshwater. During operation (middle), the top side of MHMSS was simultaneously exposed to solar irradiation and an alternating magnetic field (AMF) to enable coupled photothermal–magnetothermal energy input, while the bottom fins were immersed in water as a cold-end heat sink to maintain a low temperature and strengthen the condensation driving force. To evaluate the evaporation performance, a coupled SUN-AMF testing platform was established (right), including a solar simulator for photothermal power input, an AMF generator for magnetothermal power input, an infrared thermal camera for real-time monitoring of the top temperature field, and a computer for data acquisition and processing.

2.3. Theoretical analysis

A comprehensive theoretical analysis of the MHMSS was conducted by developing a mathematical model and performing numerical calculations. The analysis focuses on the temperature distribution, evaporation efficiency, and heat losses, and further elucidates the effects of key design parameters, input power, and ambient conditions on the overall performance. To simplify the model and highlight the dominant physical processes, the following assumptions were adopted: (1) The thermal resistances of the condensation layer and the evaporation layer are neglected; (2) Convective heat transfer inside the chamber is neglected; (3) Water vapor diffusion is modeled using pure water vapor; (4) Heat and mass transfer within the chamber are simplified as one-dimensional processes; (5) The distillation module is assumed to be sufficiently sealed, with negligible vapor leakage and condensate leakage. **(Note S1-S3).**

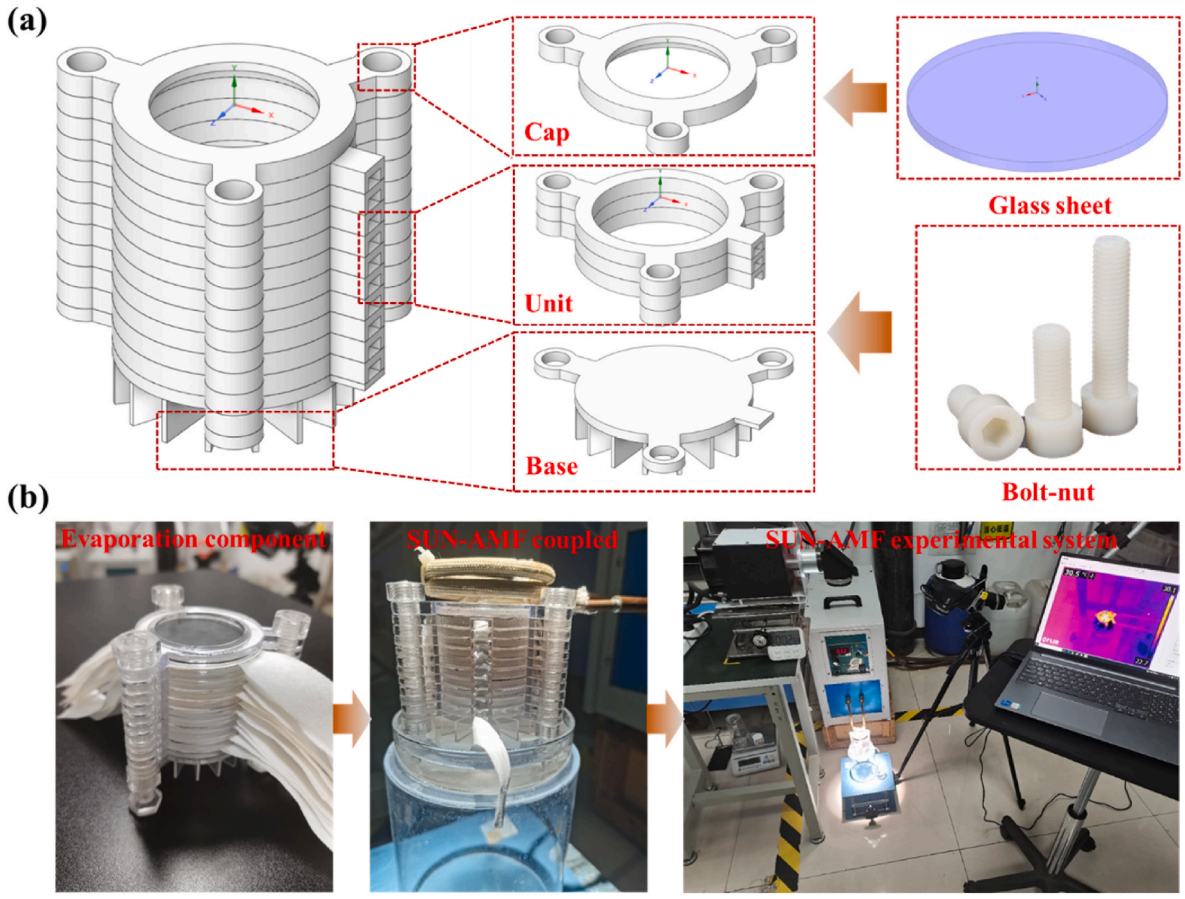

Fig. 2. Physical model, assembly configuration, and solar irradiation–alternating magnetic field (SUN–AMF) coupled experimental platform of the magnetic heat-assisted multi-stage solar still (MHMSS). (a) Physical model and system components of the MHMSS. (b) Photographs of the 3D-printed assembled device (left), the coupled photothermal–magnetothermal operation under SUN–AMF (middle), and the SUN–AMF experimental test platform (right).

2.3.1. *Mathematical model of single-stage stills*

As illustrated in Fig. 3a, the single-stage evaporation–condensation unit can be treated as a steady coupled heat and mass transfer model comprising a hot-side evaporation interface, a vapor gap, and a cold-side condensation interface. A magnetic porous carbon film located at the top serves as the energy conversion layer, generating photothermal heat under solar irradiation (q_{sun}) and magnetothermal heat under an alternating magnetic field ($q_{magnetic}$), thereby elevating the up-side temperature T_u. The supplied energy is distributed through three major pathways: (i) interfacial evaporation, producing a vapor flux J_{evap} and q_{evap}. (ii) Parasitic heat conduction q_{cond} and heat radiation q_{rad} across the vapor gap to the cold side. And (iii) heat dissipation to the ambient through the glass cover via convection and radiation, $q_{conv} + q_{rad}$. In addition, radial heat loss through the sidewall, q_{side}, is accounted for using an equivalent thermal resistance network consisting of a conductive resistance in series with an external convective resistance. Based on these heat flux pathways, the following section first establishes the energy balance equation, then formulates the expressions for the

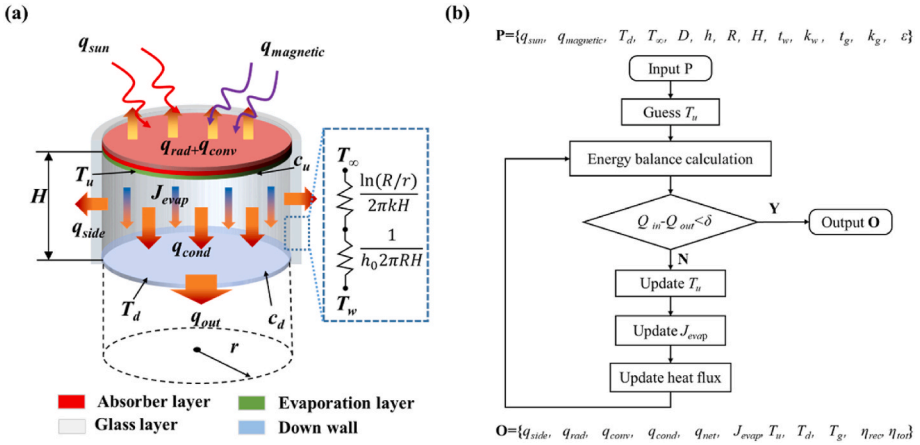

Fig. 3. Heat and mass transfer processes and computational logic of the single-stage evaporation–condensation unit. (a) Schematic illustration of the coupled heat and mass transfer in the single-stage evaporation–condensation module. (b) Flowchart of the iterative solution procedure for the single-stage model.

individual heat fluxes and the evaporation flux, and finally evaluates the single stage efficiency.

Taking the up-side evaporation interface as the control surface, the steady-state energy balance per unit area is as follows:

$$q_{in} = q_{sun} + q_{magnetic} = q_{up,loss} + q_{cond} + q_{rad} + q_{evap} = q_{out} \tag{1}$$

where q_{sun} and $q_{magnetic}$ are the equivalent photothermal and magneto-thermal heat input fluxes ($W \cdot m^{-2}$), and the $q_{magnetic}$ is calculated based on previous reports (Zhang et al., 2025, 2026). $q_{up,loss}$, q_{cond}, q_{rad} and q_{evap} represent the up-wall heat loss, heat conduction, heat radiation across the vapor gap, and the latent-heat flux associated with evaporation, respectively.

The inner-wall temperature of the glass is assumed to be equal to the hot-side interfacial temperature T_u, and the outer-surface temperature of the glass, denoted as $T_{g,out}$, is implicitly determined by enforcing energy continuity between one-dimensional heat conduction through the glass and the combined convection–radiation heat transfer at the outer surface of the glass sheet:

$$\frac{k_g}{t_g}\left(T_u - T_{g,out}\right) = h_a\left(T_{g,out} - T_\infty\right) + \varepsilon_g \sigma\left(T_{g,out}^4 - T_\infty^4\right) \tag{2}$$

Accordingly, the up-wall heat loss flux is taken as the conductive heat flux through the glass:

$$q_{up,loss} = \frac{k_g}{t_g}\left(T_u - T_{g,out}\right) \tag{3}$$

where k_g, t_g, h_a, ε_g, σ, and T_∞ are the thermal conductivity and thickness of the glass, the external convective heat-transfer coefficient, the emissivity, the Stefan–Boltzmann constant, and the ambient temperature, respectively.

When convection in the vapor gap is neglected, one-dimensional conduction across the vapor gap is as follows:

$$q_{cond} = \frac{k_a}{H}\left(T_u - T_d\right) \tag{4}$$

where H is the height of vapor-gap, k_a is the thermal conductivity, and T_d is the cold side temperature.

The radiative heat transfer between the high-temperature evaporation surface and the low-temperature condensation surface is expressed as follows

$$q_{rad} = \varepsilon_c \sigma\left(T_u^4 - T_d^4\right) \tag{5}$$

where σ is the Stefan-Boltzmann constant, and the term ε_c represents the effective emissivity.

When convective mass transfer in the vapor gap is neglected, vapor transport across the gap is dominated by diffusion (Lu et al., 2019; Zhang et al., 2020b). The q_{evap} can be calculated as follows:

$$q_{evap} = J_{evap} M_w h_{fg} \tag{6}$$

where M_w is the molar mass of water and h_{fg} is the latent heat of vaporization.

The corresponding diffusion-controlled vapor flux J_{evap} is as follows:

$$J_{evap} = \frac{D_a}{H}\left(c_u - c_d\right) \tag{7}$$

The corresponding vapor concentration is closely related to the temperature and can be further calculated as follows:

$$c_u = \frac{p_u}{RT_u}, c_d = \frac{p_d}{RT_d} \tag{8}$$

$$p_u = p_{sat}(T_u), p_d = p_{sat}(T_d) \tag{9}$$

where D_a is the diffusivity of water vapor in air, R is the universal gas constant.

Sidewall heat dissipation is modeled using a series thermal resistance network consisting of radial conduction through the insulation and external convection. Let the evaporation-area radius be R, the sidewall insulation thickness be t, the outer radius be $R_O = R + t$, and the outer lateral area be $A_o = 2\pi R_O H$.

Radial conduction resistance:

$$R_{side,cond} = \frac{\ln\left(R_o/R\right)}{2\pi k_w H} \tag{10}$$

External convective resistance:

$$R_{side,conv} = \frac{1}{h_a A_o} \tag{11}$$

The side wall temperature can be approximately regarded as the average temperature of the up wall and down wall:

$$T_{avg} = \frac{T_u + T_d}{2} \tag{12}$$

The sidewall heat loss power is

$$Q_{side} = \frac{T_{avg} - T_\infty}{R_{side,cond} + R_{side,conv}} \tag{13}$$

which can be converted into a heat flux based on $A_o = 2\pi R_O H$:

$$q_{side} = \frac{Q_{side}}{A_o} \tag{14}$$

The overall single-stage energy utilization efficiency, η_{tot}, is defined by taking the evaporative latent-heat flux q_{evap} as the useful output and normalizing it by the total input flux($q_{sun} + q_{magnetic}$), thereby quantifying the capability of converting the supplied energy into phase-change evaporation, and the η_{tot} can be calculated by the following formula:

$$\eta_{tot} = \frac{A q_{evap}}{A\left(q_{sun} + q_{magnetic}\right)} \tag{15}$$

Among them, A represents the evaporation and condensation area, which is $A = \pi R^2$.

However, not all of the heat associated with evaporation/condensation is recoverable. Owing to sidewall heat loss, a fraction of the condensation-released latent heat is dissipated to the surroundings through the sidewalls, whereas only the heat transferred toward the bottom boundary can be effectively collected and potentially reused for cascading heat recovery. Accordingly, a recoverable efficiency is further defined to evaluate the reusability of the condensation latent heat, which is calculated as follows:

$$\eta_{rec} = \frac{A q_{evap} - A_o q_{side}}{A\left(q_{sun} + q_{magnetic}\right)} \tag{16}$$

To solve the mathematical model described by Eqs. (1)–(16), an iterative solver was developed, taking the parameter set **P** as input and returning the output set **O**. As shown in Fig. 3b, the single-stage model is solved by enforcing the steady-state energy balance. A parameter set **P** (including q_{sun}, $q_{magnetic}$, T_u, T_∞, the gap height H, and the relevant thermo-physical and heat-transfer properties of air and glass) is first specified, and an initial guess for the up-side interfacial temperature T_u is prescribed. For a given T_u, all heat-transfer pathways are evaluated: the up-wall loss is obtained by implicitly solving the glass conduction and heat exchange to determine $T_{g,out}$ and thus $q_{up,loss}$. Meanwhile, the heat conduction q_{cond}, heat radiation q_{rad} across the vapor gap and the diffusion-controlled evaporation flux J_{evap}, and the associated latent-heat flux q_{evap} are updated. The total heat outflow is then compared with the input $q_{sun} + q_{magnetic}$ to form the energy balance residual, and T_u is iteratively corrected until the convergence criterion $|q_{in} - q_{out}| < \delta$ is satisfied, after convergence, T_u, $T_{g,out}$, J_{evap}, and the heat-flux components are

reported. Additionally, the sidewall heat loss q_{side} is estimated using a thermal-resistance network, based on which the overall efficiency η_{tot} and the recoverable efficiency η_{rec} are finally evaluated.

2.3.2. Mathematical model of multi-stage stills

Building upon the previously developed single-stage evaporation–condensation model, a photothermal–magnetothermal coupled multi-stage stills heat-transfer model is further established. At the first stage, the magnetic porous carbon functional layer converts incident solar irradiation and an alternating magnetic field into photothermal and magnetothermal heat inputs, thereby driving successive evaporation–condensation cycles across multiple stages for freshwater production. The bottom cold end fins are immersed in water to maintain a low temperature and provide a stable heat-sink boundary for the cascading system. With the resulting multi-stage mathematical modeling, the stage-wise temperature distribution, evaporation fluxes, and overall freshwater yield can be predicted.

For stage i ($i = 1, \cdots, n$), the cross-gap transfer capability consists of the heat conduction $q_{cond,i}$, heat radiation $q_{rad,i}$ and the evaporative latent-heat power $q_{evap,i}$. Meanwhile, the sidewall heat loss $q_{side,i}$ dissipates heat to the surroundings and reduces the net heat available for cascading. Therefore, the net output power delivered to the next stage satisfies:

$$Aq_{out,i} = Aq_{cond,i} + Aq_{rad,i} + Aq_{evap,i} - A_o q_{side,i} \tag{17}$$

In addition, a positive evaporation driving force is enforced by

$$T_{u,i} > T_{d,i} \tag{18}$$

Among them, $q_{cond,i}$ and $q_{rad,i}$ are the heat conduction and heat radiation of stage i, which can be calculated according to Eqs. (4) and (5), $q_{evap,i}$ is the evaporative latent-heat flux of stage i, which can be calculated according to Eqs. (6)–(9), and $q_{side,i}$ is the side wall heat loss of stage i, which can be calculated according to Eqs. (10)–(14).

To achieve a prescribed net output $q_{out,i}$, stage i requires an input power $q_{in,i}$ from the up stage. Since stage 1 additionally experiences heat dissipation through the glass cover, the input power is expressed as follows:

$$\begin{cases} Aq_{in,i} = Aq_{up,i} + Aq_{out,i} + A_o q_{side,i} & (i = 1) \\ Aq_{in,i} = Aq_{out,i} + A_o q_{side,i} & (i > 1) \end{cases} \tag{19}$$

Physically, internal stages allocate their input mainly to produce the net cascading output and to compensate sidewall loss, whereas the top stage must further offset the up-cover convection and radiation loss, thereby reducing the effective heat entering the cascading stack.

The multi-stage stack is coupled via ideal heat cascading through power continuity and temperature continuity:

$$q_{out,i-1} = q_{in,i}, T_{d,i-1} = T_{u,i} \tag{20}$$

where Equation (20) indicates that the net output of stage $i-1$ supplies the required input of stage i, and assumes negligible interfacial thermal resistance.

The input energy of the first stage is provided by sunlight and an alternating magnetic field as follows:

$$q_{in,1} = q_{tot} = q_{sun} + q_{magnetic} \tag{21}$$

Treating the sum of evaporative latent-heat powers across all stages as the useful output, the overall efficiency is defined as follows:

$$\eta_{tot}^{n} = \frac{\sum_{i=1}^{n} Aq_{evap,i}}{Aq_{tot}} \tag{22}$$

This metric quantifies the overall capability of converting the external input into phase-change vapor generation and is directly linked to the water-production potential.

Accordingly, the recoverable efficiency is defined as follows:

$$\eta_{rec}^{n} = \frac{\sum_{i=1}^{n} \left(Aq_{evap,i} - A_o q_{side,i} \right)}{Aq_{tot}} \tag{23}$$

By adopting a multistage latent-heat cascading strategy, the present distiller enables both the total efficiency η_{tot}^{n} and the recoverable efficiency η_{rec}^{n} to exceed 100%, as condensation heat released in one stage can be repeatedly recovered and reused to drive evaporation in downstream stages.

To quantitatively determine the effective stage number of the multi-stage distiller, the incremental gain in total efficiency caused by adding one more stage is defined as:

$$\delta_{\eta}(n) = \frac{\eta_{tot}^{n} - \eta_{tot}^{n-1}}{\eta_{tot}^{n-1}} \times 100\% \tag{24}$$

When $\delta_{\eta}(n)$ falls below a prescribed threshold, the corresponding stage number is regarded as the effective stage limit for the given configuration. In the present study, a threshold of 1% is adopted.

To solve the heat and mass transfer process of MHMSS, an iterative algorithm based on Fzero was constructed. As illustrated in Fig. 4b, the multi-stage model is solved using a power-matching, bottom-up iterative scheme that maps the input parameter set **P** to the output set **O**. For a given total input $q_{tot} = q_{sun} + q_{magnetic}$, the algorithm first initializes the boundary conditions by prescribing the cold-end temperature of the last stage, $T_d^n = T_\infty$, and assigning an initial guess for the net heat flux leaving the last stage, $q_{out,n}$. The stages are then solved sequentially from $i = n$ down to 1: at each stage, the up-side temperature $T_{u,i}$ is obtained by enforcing the stage energy balance, where the conductive heat loss $q_{cond,i}$, radiation heat loss $q_{rad,i}$, diffusion-limited evaporation flux $J_{evap,i}$, and sidewall dissipation $q_{side,i}$ are updated consistently. For the top stage ($i = 1$), a dedicated glass cover solver is additionally invoked to account for the coupled conduction and convection–radiation loss. Based on the converged stage solution, the heat-flux variables are updated and propagated to the next upstream stage until the full stack is resolved. Finally, the calculated top-stage required input $q_{in,1}$ is compared with the prescribed q_{tot}, if $|q_{in,1} - q_{tot}| < \delta$, the iteration terminates and **O** (including q_{rad}, q_{conv}, q_{cond}, q_{net}, J_{evap}, T_u, T_d, $T_{g,out}$, η_{tot} and η_{rec}) is reported. Otherwise, a global scaling factor $\gamma = q_{tot}/q_{out,n}$ is used to update the initial guess $\gamma q_{out,n} \rightarrow q_{out,n}$, and the bottom-up sweep is repeated until convergence is achieved.

2.4. Verification of heat transfer model

To validate the reliability of the proposed multi-stage evaporation–condensation model, experiments were conducted using different numbers of stages ($n = 3,5,7,10$) under $q_{sun} = 1000$ W m^{-2} and $q_{magnetic} = 226$ W m^{-2}. For the evaporation rate (Fig. 5a), the simulated values were 2.47, 3.18, 3.48, and 3.62 kg m^{-2} h^{-1}, while the corresponding experimental values were 2.39, 3.04, 3.31, and 3.43 kg m^{-2} h^{-1}. The relative deviations were 3.77%, 4.37%, 4.91%, and 5.14%, respectively, these results indicate that the model captures both the magnitude and the increasing trend in water production with increasing stage number. For the temperature prediction (Fig. 5b), the simulated upper-glass temperatures were 52.3 °C, 56.7 °C, 58.3 °C, and 59.0 °C, compared with experimentally measured values of 51.2 °C, 54.7 °C, 55.8 °C, and 57.1 °C. The corresponding relative deviations were 2.10%, 3.53%, 4.29%, and 3.22%, with an average deviation of approximately 4%. The infrared thermographs (Fig. 5c) further show that the high-temperature region is localized near the top energy-input zone, and the stage-dependent temperature evolution agrees well with the simulation trend. The experimental setup and operating configuration are shown in Fig. 5d, where the bottom cold-end fins were immersed in water to maintain a low cold-side temperature and provide a stable heat-sink boundary. Overall, the predicted evaporation rates and key temperature metrics agree well with the experiments, with deviations

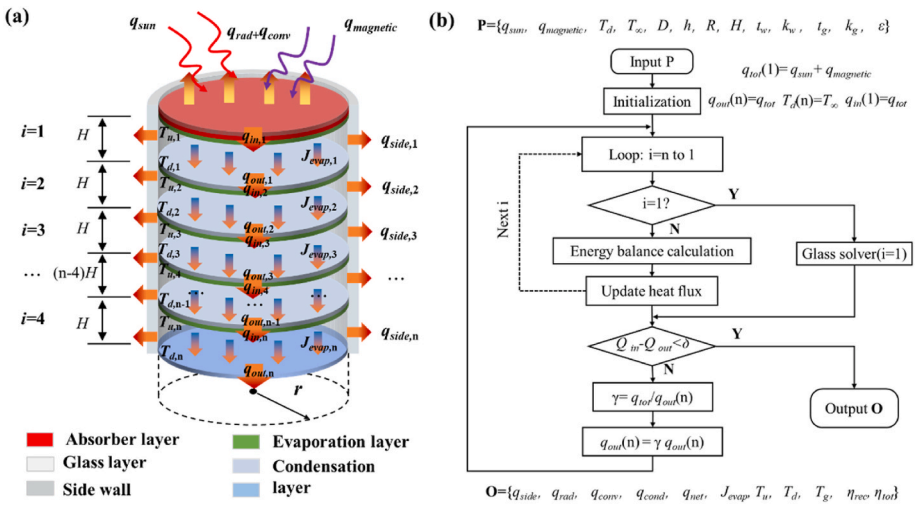

Fig. 4. Heat-transfer model and iterative solution procedure for the multi-stage evaporation–condensation system. (a) Schematic illustration of the coupled heat and mass transfer in the multi-stage stills. (b) Flowchart of the iterative calculation for the multi-stage model. This model enables prediction of the stage-wise temperature field, evaporation rate, and energy efficiency.

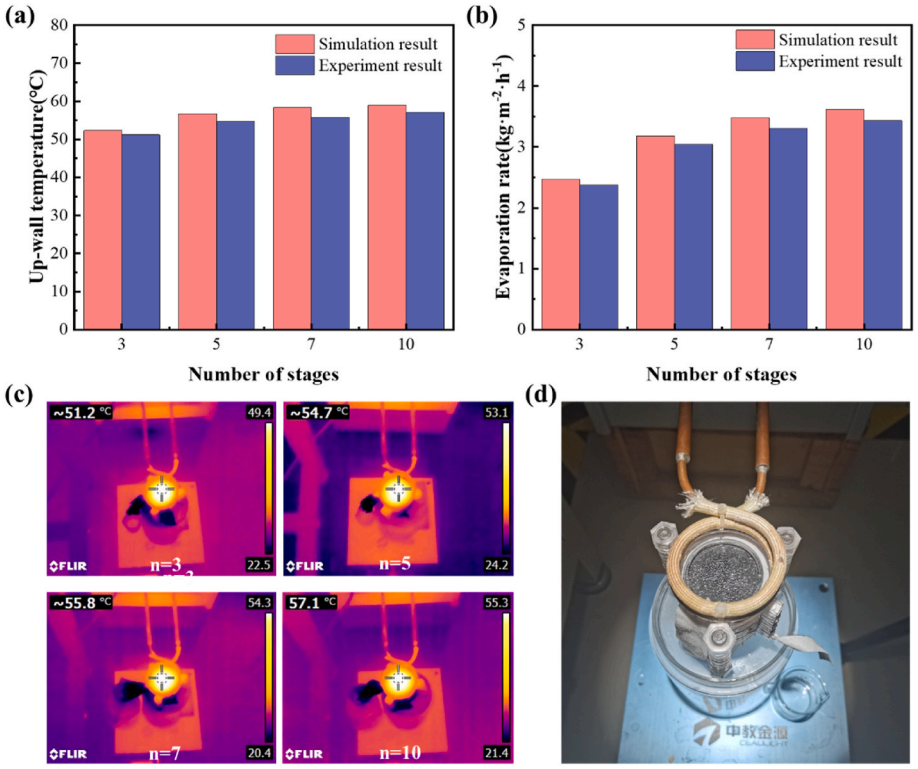

Fig. 5. Experimental validation of the multi-stage distillation model(n = 3,5,7,10). (a) Comparison of simulated and experimental evaporation rates at different stage. (b) Comparison of simulated and experimental top-surface temperatures at different stage. (c) Infrared thermographs of the top region at different stage. (d) Photograph of the multi-stage stills and the experimental test setup during operation. Test conditions: q_{sun} = 1000 W m^{-2} and $q_{magnetic}$ = 226 W m^{-2}.

confined to roughly 2-5%, confirming the validity of the model for predicting the temperature field, freshwater yield, and energy-utilization performance of the multi-stage stills. The remaining discrepancies are likely attributable to practical factors such as interfacial contact thermal resistance introduced during assembly, non-uniform sidewall heat dissipation, weak natural convection within the vapor chambers, and ambient disturbances.

3. Results and discussion

3.1. Single-stage evaporation performance

We first performed numerical simulations of the coupled heat and mass transfer in the single-stage evaporation–condensation unit, with a particular focus on the effect of the vapor-chamber height *H*. The detailed parameters used in the theoretical calculations are provided in Table S1. As shown in Fig. 6, the evaporation rate (Fig. 6a), upper-wall temperature (Fig. 6b), heat flux (Fig. 6c), and energy efficiency (Fig. 6d)

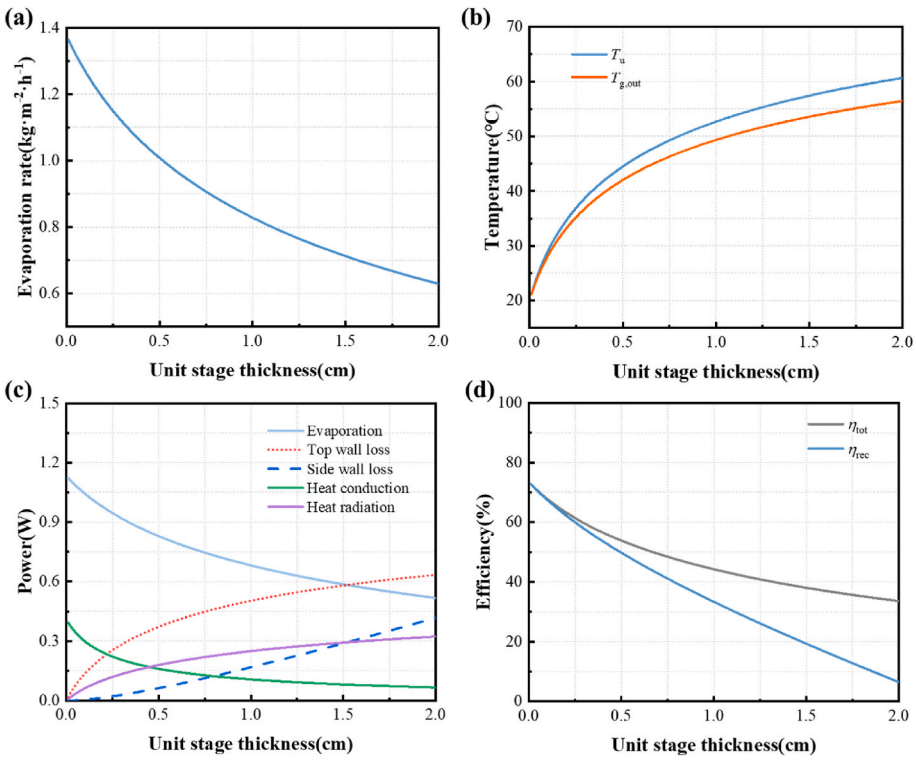

Fig. 6. Numerical results of the single-stage evaporation–condensation unit. (a) Evaporation rate derived from the evaporation flux. (b) Upper-wall temperature T_u and outer-glass-surface temperature $T_{g,out}$. (c) Contributions of different heat flux pathways. (d) Total evaporation efficiency and recoverable efficiency. The chamber height H is varied from 0 to 2.0 cm, demonstrating that H plays a critical role in governing the temperature levels, evaporation rate, heat losses, and efficiency.

are obtained for different chamber heights H.

Fig. 6a–d collectively quantify the coupled heat and mass transfer response of a single-stage evaporation–condensation unit to the vapor-chamber height H under an input power of 1226 W m^{-2}. As H increases, the evaporation rate decreases monotonically (Fig. 6a), dropping from 1.36 kg $m^{-2}{\cdot}h^{-1}$ to 0.62 kg $m^{-2}{\cdot}h^{-1}$. According to Eq. (7), enlarging H increases the diffusion-controlled mass transfer resistance approximately linearly, which suppresses vapor transport. Although the upper-wall temperature T_u rises with H, thereby enhancing the evaporation driving force through the nonlinear increase of the saturation vapor concentration, this gain is insufficient to offset the geometric penalty, leading to a net reduction in evaporation flux. As shown in Fig. 6b, both up wall temperature T_u and the outer glass temperature $T_{g,out}$ increase monotonically with H, while a persistent temperature gap remains between them, primarily due to the thermal resistance of the glass cover. The energy distribution in Fig. 6c further reveals that, in the limit $H\to0$, cross-gap conduction dominates (0.39 W), indicating a pronounced sensible-heat short-circuit. With increasing in H, the heat conduction decreases rapidly following the intrinsic $1/H$ scaling to 0.06 W at $H = 2$ cm, whereas cross-gap heat radiation becomes increasingly important and approaches a plateau as the temperature rises. Meanwhile, external dissipation through the top cover and sidewall increases steadily with H and becomes a major penalty at large gaps, giving 0.63 W for the top loss and 0.41 W for the sidewall loss at $H = 2$ cm, thereby undermining effective energy utilization. Consistently, Fig. 6d shows that both the total efficiency η_{total} and the recoverable efficiency η_{rec} decline with H, where η_{tot} drops from 72.79% to 33.59%, while η_{rec} decreases from 72.79% to 6.47% at large H. Overall, under the present conditions, reducing H is favorable for alleviating diffusion limitations and suppressing boundary heat losses, thereby improving evaporation and efficiency.

3.2. Multi-stage evaporation performance

To enhance heat recovery and thereby increase freshwater production, a multi-stage evaporation–condensation module was constructed to analyze the coupled heat and mass transfer in the MHMSS (Fig. 4). Unless otherwise specified, all parameters were kept identical to those used in the single-stage model (Table S1). A representative case with $n =$ 16 stages and a chamber height of $H = 0.4$ cm was adopted for the following analysis. As evidenced by Fig. 7a–c, the MHMSS exhibits a pronounced front-loaded evaporation behavior, where the upstream stages dominate the overall vapor generation while the downstream stages contribute marginally. In Fig. 7a, the stage-wise evaporation rate decreases rapidly with increasing stage number, from 0.91 kg m^{-2} h^{-1} at stage 1 to only 0.05 kg m^{-2} h^{-1} at stage 10, indicating that effective evaporation is largely confined to the first several stages. This decay is consistent with the cascading temperature drop shown in Fig. 7b, the upper-wall temperature T_u decreases from 63.7 °C at stage 1 to 25.5 °C at stage 10, which substantially reduces the driving force for diffusion-controlled evaporation $\Delta c = c_{sat}(T_u) - c_{sat}(T_d)$, and thereby suppresses the vapor flux according to $J_{evap}\propto D_a\Delta c/H$. Meanwhile, the outer-surface temperature of the glass cover is 59.16 °C, remaining lower than the stage-1 up-side temperature and thus reflecting the insulating role of the glass in mitigating top-surface convection and radiation losses. Fig. 7c further rationalizes the stage to stage attenuation from an energy allocation perspective. At stage 1, only 44.7% of the input power is transferable to the next stage, while 44.5% is dissipated through the top wall and 10.9% through the sidewall (Pie chart illustration). Although the top wall loss vanishes in internal stages, sidewall dissipation persists along the cascade and continuously extracts the transferable heat, leading to a rapidly diminishing heat input to downstream stages and an insufficient temperature head to sustain appreciable evaporation. Overall, the top cover of Stage 1 is a critical thermal bottleneck in the present design, and further reduction of this loss through improved cover insulation will be an important direction for future optimization.

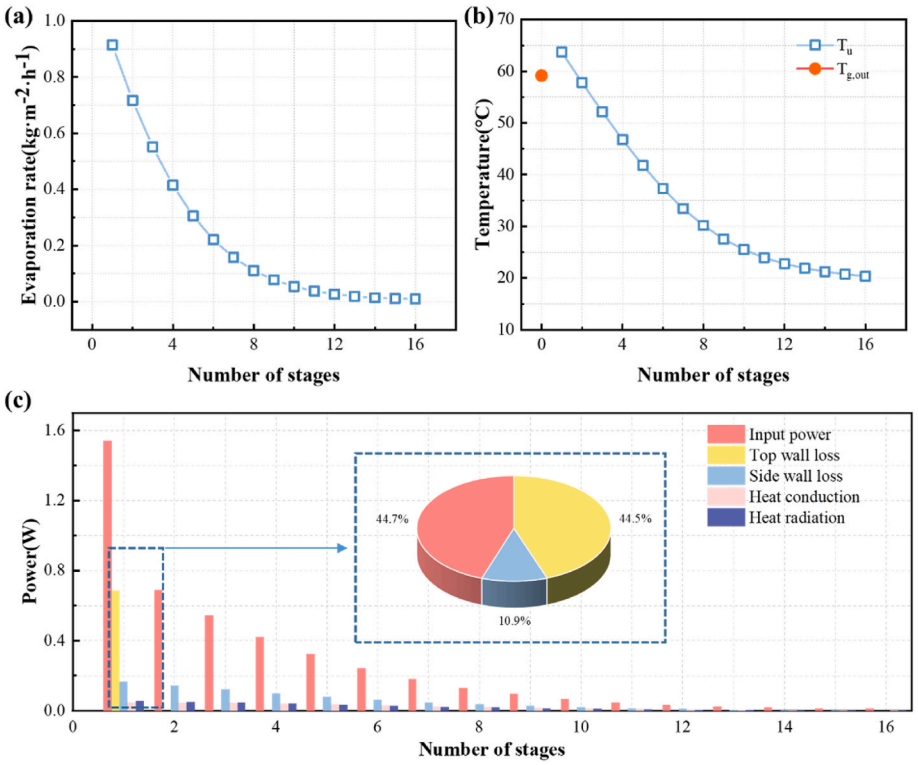

Fig. 7. Heat and mass transfer results of the 16-stage MHMSS. (a) Stage-wise variation in evaporation rate. (b) Stage-wise variation in upper-wall temperature. (c) Distribution of heat-loss components across stages. The inset pie chart shows the energy partitioning for stage 1. Simulation conditions: $n = 16$ and $H = 0.4$ cm.

Based on the current results, the heat and mass transfer processes of MHMSS under different total series were further explored. Fig. 8 collectively demonstrates that increasing the stage number strengthens latent-heat cascading in the MHMSS, while a clear diminishing behavior

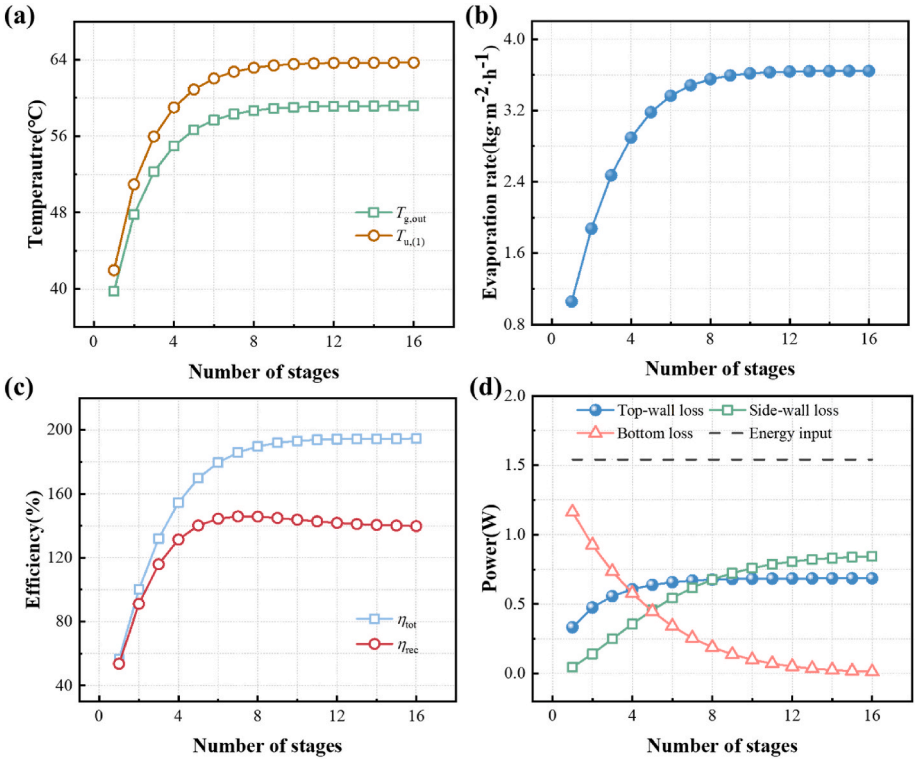

Fig. 8. Cumulative evaporation performance and energy efficiencies of the MHMSS. (a) Variation of the Stage-1 upper-wall temperature T_u and the outer-glass-surface temperature $T_{g,out}$. (b) Cumulative evaporation rate. (c) Cumulative total efficiency η_{tot} and recoverable efficiency η_{rec}. (d) Evolution of cumulative heat losses with stage number. The total stage number n increases from 1 to 16.

emerges. The temperature response in Fig. 8a shows that both the up-wall temperature T_u and the outer-glass surface temperature $T_{g,out}$ rise rapidly with n and approach plateaus for $n = 10$, approximately 63.54 °C for T_u and 59.02 °C for $T_{g,out}$, indicating that enhanced cascading enables a higher and more stable effective temperature head under the same external input. The persistent offset $T_{g,out} < T_u$ further reflects the thermal resistance of the glass cover, which suppresses top-surface convection–radiation exchange and favors internal heat recirculation. Accordingly, the overall evaporation rate increases markedly but gradually saturates (Fig. 8b), the evaporation rate rises from 1.05 kg m^{-2} h^{-1} at $n = 1$ to 3.62 kg m^{-2} h^{-1} around $n = 10$, beyond which additional stages offer limited gains, implying an upper bound of effective working stages for the present configuration. As shown in Fig. 8c, the efficiency metrics exhibit a similar plateau trend, where the η_{tot} increases from 56.51% to 194.56% and levels off at larger n, highlighting the substantial heat gain enabled by repeated evaporation heat reuse, whereas η_{rec} reaches 143.81% at $n = 10$ and then remains close to 139.81%, suggesting that the recoverable contribution becomes increasingly constrained by parasitic dissipation at higher n. Finally, the evolution of energy partitioning provides a mechanistic explanation for the observed saturation. As shown in Fig. 8d, at low stage number n, the bottom loss is dominant (1.1−1.2 W), indicating that a large fraction of evaporation heat is discharged without being cascaded. With increasing n, this term decreases rapidly and becomes nearly negligible at high n, directly driving the rise in evaporation rate and η_{tot}. Meanwhile, adding stages increases the effective sidewall heat-transfer area and the overall heat-transfer path length, causing the sidewall loss to plateau at 0.8 W, while the top-wall loss also increases and stabilizes at 0.6−0.7 W. Overall, for the present geometry, the effective stage limit appears at about $n = 10$ because the benefit of further suppressing bottom heat loss is nearly exhausted by this point, whereas the cumulative sidewall dissipation and the large Stage-1 top-wall loss already consume most of the transferable heat. As a result, the additional downstream stages receive insufficient thermal driving force to sustain appreciable evaporation, leading to the observed plateau in evaporation rate and efficiency.

3.3. Effect of structural parameters

Based on this, we explored the effect of chamber height H, evaporation surface radius R and side wall thickness t. Fig. 9 provides a systematic parametric assessment of how key geometric factors govern latent-heat cascading and freshwater production in the MHMSS. For n = 1–16, the cumulative efficiencies η_{tot} and η_{rec}, cumulative evaporation rate, and heat loss are compared.

As shown in Fig. 9a and b, the chamber height H strongly governs cascaded heat and mass transfer in the MHMSS. Decreasing H increases both the cumulative evaporation rate and the cumulative efficiencies and allows the system to reach the plateau with fewer stages. With a H of 0.2 cm, η_{tot} reaches 378.00% and η_{rec} reaches 333.75%, this behavior

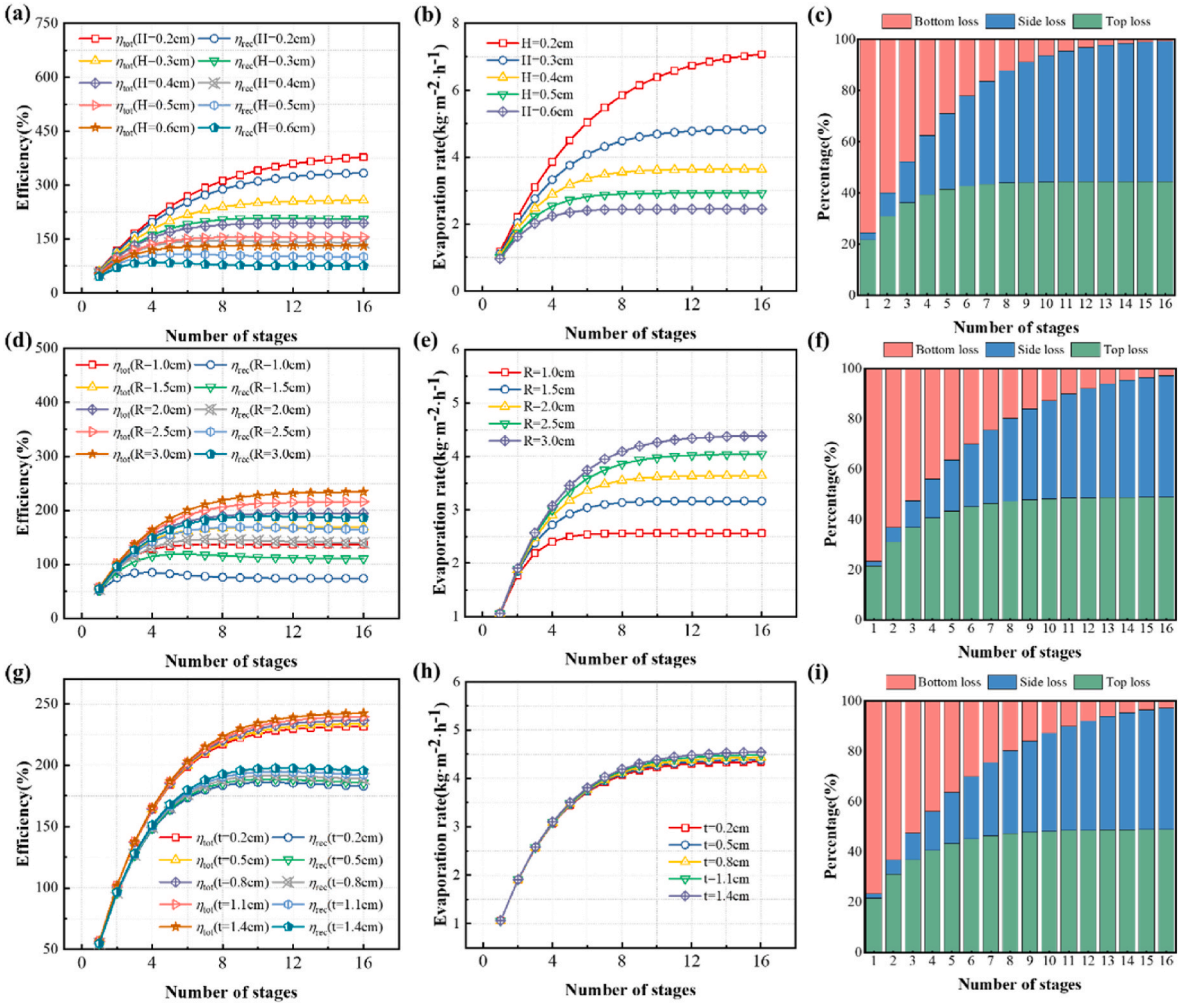

Fig. 9. Effects of key geometric parameters on the performance of the MHMSS. (a-c) Cumulative efficiencies, cumulative evaporation rate, and heat-loss partitioning under different chamber heights H. (d-f) Cumulative efficiencies, cumulative evaporation rate, and heat-loss partitioning under different evaporation-surface radius R. (g-i) Cumulative efficiencies, cumulative evaporation rate, and heat-loss partitioning under different sidewall thicknesses t.

stems from the geometric sensitivity of diffusion controlled evaporation. A smaller H reduces mass transfer resistance and improves the utilization of transferable heat along the cascade, and the recyclable heat includes phase change latent heat as well as the energy delivered across the gap by heat conduction and radiative exchange. The energy partitioning in Fig. 9c and Fig. S3 show that the bottom heat loss fraction decreases rapidly with stage number and becomes nearly negligible, whereas the fractions of top and side losses increase and dominate at large stage numbers. As a result, once bottom heat loss is largely suppressed, the plateau is primarily determined by parasitic boundary dissipation. An excessively small H may also compromise condensate quality, and based on the wastewater treatment validation, H equal to 0.4 cm is recommended for subsequent analyses (Figs. S4 and S5). As shown in Fig. 9d–f, increasing the evaporation-surface radius R markedly enhances both the cumulative evaporation rate and the cumulative efficiencies, and the plateau values increase monotonically with R. For example, at $R = 3.0$ cm, η_{tot} and η_{rec} reach 234.16% and 185.78%, respectively, with a cumulative evaporation rate of 4.38 kg m^{-2} h^{-1}, this improvement is primarily attributed to the geometric scaling of parasitic sidewall dissipation. For a cylindrical configuration, the effective evaporation area is $A_{face} = \pi R^2$, whereas the sidewall area can be approximated as $A_{side} = 2\pi(R + t)H$, yielding $A_{side}/A_{face} \sim 2H/R$. As a result, a larger R reduces the sidewall edge-loss burden per unit evaporation area, allowing a greater fraction of the input energy to be converted into phase-change latent heat and cascaded to downstream stages. The energy partitioning in Fig. 9f and Fig. S6 confirms that bottom heat loss is progressively suppressed as stage number increases, while top and side losses rise and then plateau. A larger R leads to a lower plateau level of side loss, supporting higher evaporation and energy efficiency. Once bottom heat loss is largely minimized, the residual top and side losses ultimately govern saturation. Fig. 9g–i indicate that increasing the sidewall thickness t enhances multistage performance mainly by strengthening sidewall insulation and suppressing sidewall dissipation. Consequently, its impact is more pronounced on efficiency metrics than on the evaporation rate. In Fig. 9h, the cumulative evaporation rate curves for different t are very close, with a plateau around 4.3 to 4.6 kg m^{-2}·h^{-1}. In contrast, Fig. 9g shows that both η_{tot} and η_{rec} shift upward with increasing t, reaching about 242.46% to 195.55% at the plateau. Mechanistically, sidewall loss is governed by radial conduction combined with external convection. Increasing t raises the radial thermal resistance and reduces sidewall heat loss, retaining more energy and directly benefiting the efficiency. As shown in Fig. 9i and Fig. S7, once bottom heat loss becomes nearly negligible at sufficiently large stage number, the system enters a plateau stage dominated by parasitic top and side losses. Consequently, the marginal benefit of further increasing t diminishes and is ultimately capped by top wall dissipation. Overall, reducing H strengthens diffusion-limited evaporation and cascaded heat recovery but may introduce water quality risks when the gap becomes too small. Increasing R mitigates the sidewall loss burden per unit evaporation area and elevates plateau performance, while increasing t mainly improves efficiency by suppressing sidewall dissipation, with increasing stage number, the controlling limitation shifts from bottom heat loss to parasitic top and side heat losses, providing physically grounded guidance for geometric design and stage number configuration.

3.4. Effect of operating conditions

Under solar irradiation, the MHMSS can change freshwater production by regulating the magnetothermal contribution to the total input heat flux. As the total input heat flux increases from 1226 W m^{-2} to 2130 W m^{-2}, the cumulative evaporation rate rises rapidly with stage number and then approaches a plateau (Fig. 10a). At a total input power of 2130 W m^{-2}, the total efficiency η_{tot} and recoverable efficiency η_{rec} reach 335.29% and 283.82%, with an evaporation rate of 10.91 kg m^{-2} h^{-1}, indicating that stronger heat input establishes a larger evaporation driving force in upstream stages and sustains more effective inter-stage energy transfer. The temperature response in Fig. 10b shows that the characteristic temperature increases with stage number and gradually

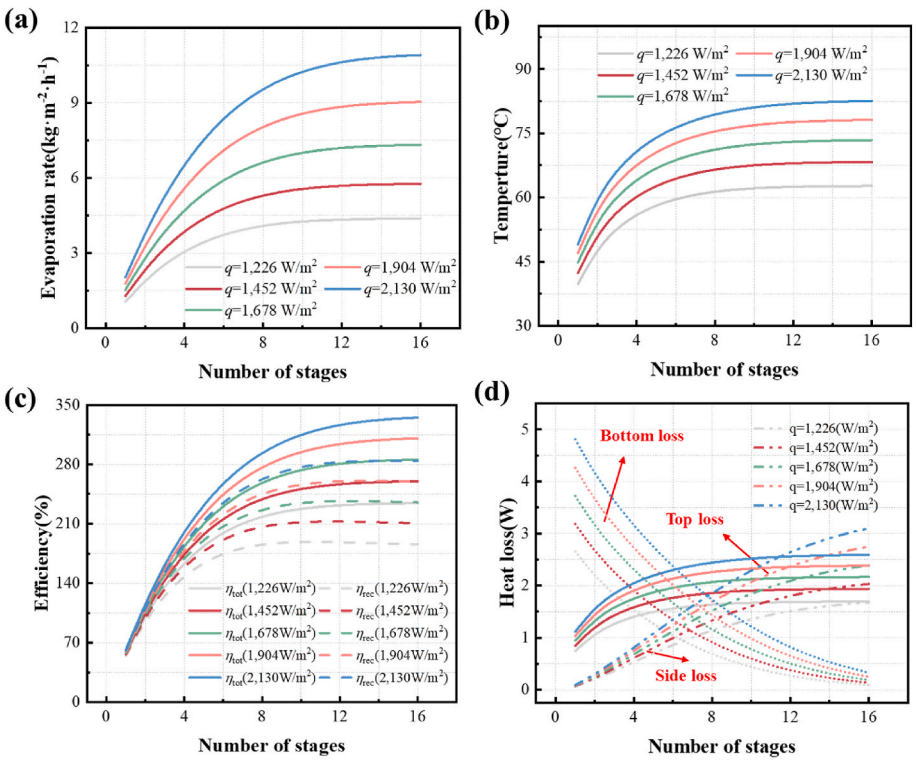

Fig. 10. Effects of input energy on the performance of the MHMSS. (a) Cumulative evaporation rate. (b) Outer-glass-surface temperature $T_{g,out}$. (c) Cumulative total efficiency η_{tot} and cumulative recoverable efficiency η_{rec}. (d) Cumulative heat-loss, including top heat loss, side heat loss, and bottom heat loss.

stabilizes, while the steady plateau shifts upward monotonically with increasing input heat flux. At sufficiently large stage numbers, the temperature plateau increases from about 62.71 °C to about 82.55 °C, implying that the upper steady temperature is primarily dictated by boundary dissipation and is pushed to a higher level as the input increases. Fig. 10c further indicates that both the cumulative total efficiency and the cumulative recoverable efficiency shift upward with increasing input flux, yet still exhibit saturation with stage number, suggesting that multistage reuse significantly improves energy utilization but the ultimate gain remains constrained by parasitic losses. Fig. 10d provides the energy basis for this limitation, the bottom heat loss dominates at low stage numbers, reflecting substantial terminal heat loss that has not been effectively cascaded. With increasing stage number, bottom loss decreases rapidly, whereas top and side losses increase and become the primary dissipation channels at large stage numbers. As a result, higher input flux amplifies the absolute magnitudes of top and side losses and causes the transition to a boundary loss dominated plateau to occur earlier, thus higher input flux delivers a pronounced productivity gain, while efficiency improvement is ultimately capped by top and side dissipation (Fig. S8). Overall, increasing the input power effectively boosts the temperature and freshwater productivity, but further gains require suppressing top and side heat losses or strengthening bottom heat recovery.

As environment temperature T_∞ increases, the cumulative evaporation-rate curves shift upward and gradually approach a plateau (Fig. 11a), while the $T_{g,out}$ increases monotonically (Fig. 11b). This indicates an elevated up-side temperature and a higher saturation vapor pressure, which strengthens the evaporation driving force and enhances cumulative freshwater productivity. Consistently, both η_{tot} and η_{rec} increase with T_∞ and exhibit higher plateau values (Fig. 11c), suggesting that a higher ambient temperature suppresses ineffective heat loss to the surroundings and allows a larger fraction of the input energy to be retained and utilized as recoverable cascade heat. Fig. 11d provides the energetic basis for this trend, increasing T_∞ reduces the boundary temperature difference ($T_{g,out} - T_\infty$), thereby decreasing or slowing the growth of the top and side heat-loss, whereas the bottom heat loss remains more dominant over the upstream stages and persists over a broader stage range. The combined effect yields a concurrent improvement in evaporation performance and efficiency, indicating higher T_∞ may also reduce the cooling margin at the cold end. Therefore, the condenser-side heat dissipation should be properly matched to avoid condensation-limited operation under warm-ambient conditions.

In solar multi-stage distillation, the external heat-transfer coefficient h essentially quantifies the intensity of heat dissipation to the surroundings and thus serves as a key boundary condition governing temperature establishment and heat recovery. To relate the external heat-transfer coefficient to practical ambient conditions, the commonly adopted engineering relation $h = 5.7 + 3.8v$ was used, the three representative values considered here, h = 5, 10, and 15 W m^{-2}, approximately correspond to near-stagnant air (v = 0 m s^{-1}), weak breeze (v = 1.1 m s^{-1}), and moderate weak breeze (v = 2.4 m s^{-1}), respectively. As shown in Fig. 12, increasing h from 5 to 15 W/m^2·K markedly reduces the cumulative evaporation rate and causes an earlier plateau (Fig. 12a), while the outer-glass surface temperature $T_{g,out}$ decreases substantially (Fig. 12b). This indicates that a larger h enhances external heat exchange, depresses the steady-state hot-side temperature, and weakens the saturation vapor pressure and concentration difference, thereby reducing the evaporation driving force and the associated evaporation heat flux. Consistently, both η_{tot} and η_{rec} decrease with increasing h (Fig. 12c), implying that stronger external heat dissipation reduces the fraction of input energy available for effective cascading. The heat-term decomposition in Fig. 12d further clarifies the mechanism, at higher h the top and sidewall loss terms increase more rapidly and dominate at lower stage numbers, prematurely extracting cascadeable bottom heat in the upstream stages and leaving insufficient driving energy for downstream stages. In contrast, a smaller h suppresses

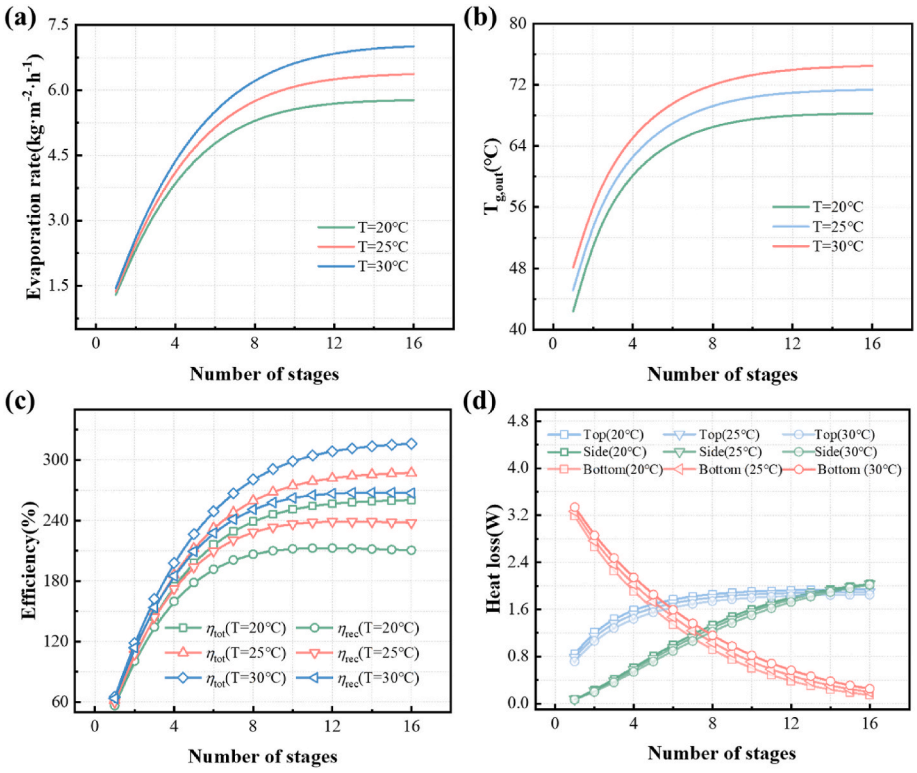

Fig. 11. Effects of ambient conditions on the performance of the MHMSS. (a) Cumulative evaporation rate. (b) Outer-glass surface temperature $T_{g,out}$. (c) Cumulative total efficiency η_{tot} and cumulative recoverable efficiency η_{rec}. (d) Evolution of heat terms with stage number, including top heat loss, sidewall heat loss, and the bottom heat loss.

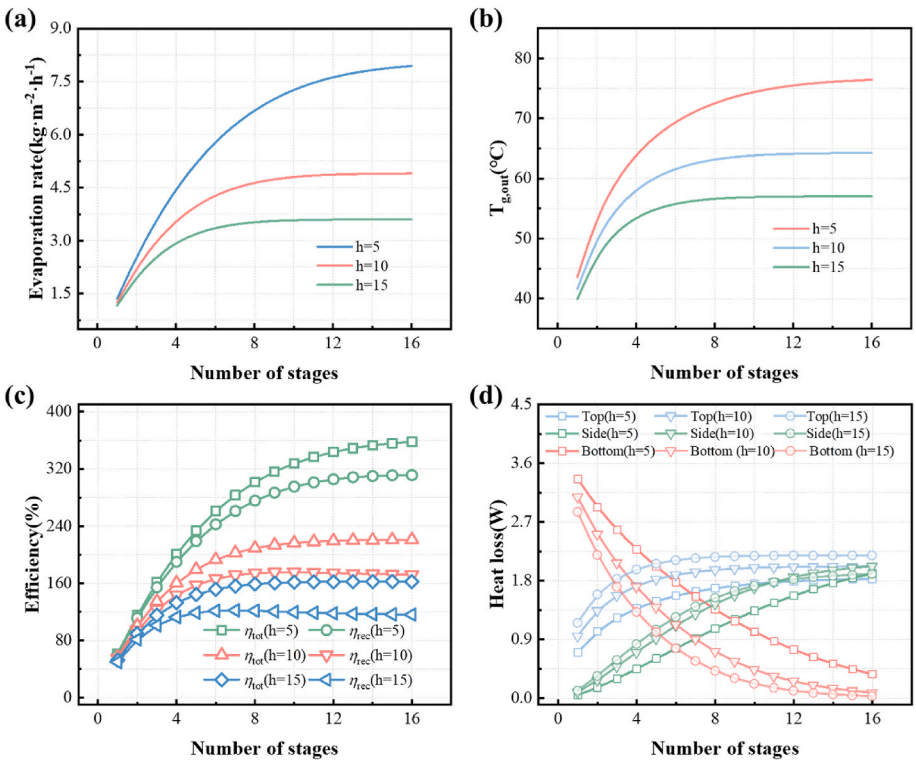

Fig. 12. Effects of heat-transfer coefficients during operation on the performance of the MHMSS. (a) Cumulative evaporation rate. (b) Outer-glass-surface temperature $T_{g,out}$. (c) Cumulative total efficiency η_{tot} and cumulative recoverable efficiency η_{rec}. (d) Evolution of major heat terms with stage number, including bottom heat loss, top heat loss, and sidewall heat loss.

these parasitic pathways, allowing a larger portion of the input energy to enter the evaporation term and be transferred stage by stage, resulting in higher evaporation-rate and efficiency plateaus. Overall, reducing the effective h is beneficial for maximizing the heat recovery advantage of multi-stage architectures.

An economic feasibility assessment was conducted by combining the manufacturing cost with the operating energy expense of the MHMSS. The fabrication cost of the evaporator is estimated to be 950 RMB/m^{-2}, as summarized in Table S2. Table 1 reports the operating-cost evaluation for the evaporation process at an energy-recovery efficiency of 300%. Under a daily solar irradiation of 4.5 kWh, the solar-only mode produces 21.54 L of freshwater (Zhang et al., 2020a). In the combined solar and alternating magnetic field mode, the freshwater yield increases to 40.69 L, but the alternating magnetic field requires an additional electricity consumption of 4.0 kWh. Using an electricity price of 0.41 RMB/kWh, the corresponding energy cost is 1.64 RMB (Xia et al., 2022). Although auxiliary power input increases the operating expense, the resulting cost per liter remains well below typical retail prices of drinking water. This cost can be further reduced by integrating renewable electricity or exploiting off-peak tariffs (Zhang et al., 2026). An extended preliminary economic analysis considering the amortized capital cost of the AMF unit was further provided in Note S4. The results show that, even after including the amortized capital cost of the AMF unit, the water-production cost in the SUN–AMF mode is still only about 0.148 RMB·L^{-1}, indicating that the overall cost remains at a relatively low level. Overall, the MHMSS enables a flexible production strategy by operating in solar-only mode under abundant sunlight and switching to the solar–magnetothermal mode under low-irradiance conditions or at night, thereby supporting low-cost freshwater production with tunable productivity.

Table 1
Economic evaluation of magnetic heat-assisted multi-stage solar stills.

Condition	Daily irradiation (kWh)	Daily consumption (kWh)	Energy cost (RMB)	water yield (L)
SUN-only	4.5	/	/	21.54
SUN-AMF	4.5	4	1.64	40.69

4. Conclusion

In this work, we developed a photothermal–magnetothermal dual-input magnetic heat-assisted multi-stage solar still (MHMSS) and established a comprehensive theoretical framework to elucidate coupled heat and mass transfer, temperature evolution, and energy allocation in multistage cascading distillation. The main conclusions are summarized as follows.

(1) The model predictions agree well with experimental measurements, with relative deviations of 3.77%–5.14% for the evaporation rate and 2.10%–4.29% for the top temperature, confirming the reliability of the proposed model in predicting the temperature distribution, evaporation rate, and energy efficiency.
(2) The single-stage analysis indicates that reducing the vapor-chamber height H suppresses overall heat losses and improves energy utilization. Multi-stage simulations further reveal a pronounced upstream-dominated evaporation behavior with clear diminishing as stage number increases: the evaporation rate decays from 0.91 kg m^{-2} h^{-1} to 0.05 kg m^{-2} h^{-1}, and heat dissipation through the top wall and sidewall is identified as the primary factor limiting the effective working stages.
(3) Regarding structural parameters, decreasing H strengthens diffusion-controlled evaporation and promotes evaporation-heat cascading, but an excessively small gap may induce back-mixing/entrainment in the condensation region and contaminate the condensate. Considering both efficiency and water quality, $H = 0.4$ cm is identified as a favorable choice. Increasing

the evaporation-surface radius R effectively improves both cumulative evaporation rate and efficiencies, at $R = 3.0$ cm, η_{tot} and η_{rec} reach 234.16% and 185.78%, with a cumulative evaporation rate of 4.38 kg m^{-2} h^{-1}. In addition, increasing the sidewall thickness t suppresses sidewall loss by enhancing the thermal resistance, leading to a more pronounced improvement in efficiency.

(4) The phase-change driving force can be effectively adjusted by varying the magnetothermal input, when the total input heat flux increases to 2130 W m^{-2}, the total efficiency η_{tot} and recoverable efficiency η_{rec} reach 335.29% and 283.82%, with an evaporation rate of 10.91 kg m^{-2} h^{-1}. Higher ambient temperature reduces heat-loss driving forces, increases the steady-state temperature and enhances productivity and efficiency, whereas a larger external heat-transfer coefficient h increases top/side losses and diminishes the benefit of evaporation-heat cascading.

CRediT authorship contribution statement

Chenghua Zhang: Writing – original draft, Validation, Software, Investigation, Data curation, Conceptualization. **Yunfei Yan:** Funding acquisition, Formal analysis. **Yonghong Wu:** Software, Data curation. **Zikang Niu:** Data curation. **Wen Siang Lew:** Writing – review & editing, Formal analysis.

Declaration of competing interest

The authors declare that they have no known competing financial interests or personal relationships that could have appeared to influence the work reported in this paper.

Acknowledgements

This work was supported by Project supported by the graduate research and innovation foundation of Chongqing, China (Grant No. CYB25027) and the China Scholarship Council (Grant No. 202506050076).

Appendix A. Supplementary data

Supplementary data to this article can be found online at https://doi.org/10.1016/j.jclepro.2026.148565.

Data availability

Data will be made available on request.

References

Chang, K.-F., Li, Y.-Z., Xi, Y.-A.-M., Xu, J.-L., Zhang, Y., 2024. Key technology developments for solar-driven interfacial evaporation in terms of structural innovation and thermal design. Nano Energy 132, 110369.
Cheng, S., He, E., Zhang, P., Sutar, R.S., Kannan, S.K., Balu, S.K., Zhao, H., Xing, R., Liu, S., 2025. Scallion-inspired environmental energy enhanced solar evaporator with integrated water transport and thermal management. Adv. Funct. Mater. 35 (26), 20243011.
Chiavazzo, E., Morciano, M., Viglino, F., Fasano, M., Asinari, P., 2018. Passive solar high-yield seawater desalination by modular and low-cost distillation. Nat. Sustain. 1 (12), 763–772.
Cui, Y., Liang, X., Wang, Y., Wang, J., Lohwacharin, J., Lichtfouse, E., Wang, C., 2025. Advances in hydrogel-based photothermal interfacial solar steam generation: classifications, mechanisms, and applications. Adv. Funct. Mater., 2509130
Deng, W., Fan, T., Li, Y., 2022. Water wave vibration-promoted solar evaporation with super high productivity. Nano Energy 92, 106745.
Du, J., Fang, H., Ma, J., Lin, J., Li, S., Jiang, Y., Huang, F., 2025. Synergistic solar-magnetic desalination via covalently anchored Fe_3O_4/hydrogel composites. Chem. Eng. J. 522, 167767.
Fang, H., Ma, J., Lin, J., Du, J., Li, S., Zhang, H., Huang, F., 2024. Electrothermal-assisted all-weather solar steam generator based on hydrogel implantation strategy. Chem. Eng. J. 494, 153110.
Fujiwara, M., Kikuchi, M., 2017. Solar desalination of seawater using double-dye-modified PTFE membrane. Water Res. 127, 96–103.
Jiang, N., Xie, Z., Wu, R., Ouyang, Z., Liu, H., Zhuo, X., Chen, A., Wang, S.B., 2025. Photothermal heat-storage nanostructure-assisted water-electricity cogeneration system with dual solar energy inputs and high-efficiency heat utilization. Adv. Funct. Mater., e14363
Li, Z., Xu, X., Sheng, X., Lin, P., Tang, J., Pan, L., Kaneti, Y.V., Yang, T., Yamauchi, Y., 2021. Solar-powered sustainable water production: State-of-The-Art technologies for sunlight-energy-water nexus. ACS Nano 15 (8), 12535–12566.
Li, Y., Wu, T., Shen, H., Yang, S., Qin, Y., Zhu, Z., Zheng, L., Wen, X., Xia, M., Yin, X., 2022. Flexible MXene-based janus porous fibrous membranes for sustainable solar-driven desalination and emulsions separation. J. Clean. Prod. 347, 131324.
Li, J., Liu, Q., He, J., Zhang, Y., Mu, L., Zhu, X., Yao, Y., Sun, C.-L., Qu, M., 2024. Aerogel-based solar interfacial evaporation: current research progress and future challenges. Desalination 569, 117068.
Liu, S., Li, S., Lin, M., 2023. Understanding interfacial properties for enhanced solar evaporation devices: from geometrical to physical interfaces. ACS Energy Lett. 8 (4), 1680–1687.
Liu, H., Wu, F., Liu, X.Y., Yu, J., Liu, Y.T., Ding, B., 2023. Multiscale synergetic bandgap/structure engineering in semiconductor nanofibrous aerogels for enhanced solar evaporation. Nano Lett. 23 (24), 11907–11915.
Liu, Y., Wang, J., Zhou, R., Ding, Z., Gu, Y., Bai, B., Sun, C., 2024. Innovations and challenges in large-area graphene oxide membranes for seawater desalination: preparation techniques, bottlenecks, and module developments. Desalination 592, 118177.
Liu, M., Sun, Y., Shao, K., Li, N., Li, J., Murto, P., Wang, Z., Chen, J., Xu, X., 2024. Synergistic solar-powered water-electricity generation: an integrated floating system on water. Nano Energy 119, 109074.
Liu, J., Zhang, S., Wang, J., Lan, Q., 2025. Recent progress in solar-driven interfacial evaporation: evaporators, condensers, applications and prospects. Desalination 597, 118356.
Lu, Z., Kinefuchi, I., Wilke, K.L., Vaartstra, G., Wang, E.N., 2019. A unified relationship for evaporation kinetics at low mach numbers. Nat. Commun. 10 (1), 2368.
Lu, T., Wu, Q., Zhou, Y., Wang, X., Shi, W., 2025. Janus membranes with dynamically reversible solar evaporation interfaces. npj Clean Water 8 (1), 84.
Luo, X., Jiao, L., Guo, Y., Bao, H., Zhao, C., Gu, X., 2024. Ultrahigh freshwater production achieved by unidirectional heat transfer interfacial evaporation solar still integrated with waste heat recovery. Energy Convers. Manag. 304, 118226.
Ma, C., Liu, Q., Peng, Q., Yang, G., Jiang, M., Zong, L., Zhang, J., 2021. Biomimetic hybridization of Janus-like graphene oxide into hierarchical porous hydrogels for improved mechanical properties and efficient solar desalination devices. ACS Nano 15 (12), 19877–19887.
Ma, W., Nie, Y., Cao, W., Fan, Q., Wen, J., Zhang, Y., Xiong, R., Huang, C., 2025. Bioinspired, robust wood solar evaporator with scale-like surfaces for efficient solar-driven water purification and thermoelectric generation. Chem. Eng. J. 519, 165196.
Miao, J., Lv, F., Gulfam, R., Zhao, W., 2023. Synergistic effect of superhydrophilic skeleton decorated with hierarchical micro/nanostructures and graphene oxide on solar evaporation. Appl. Energy 350, 121779.
Shi, L., Tao, W., Zheng, N., Zhou, T., Sun, Z., 2023. Magnetic photo-thermal evaporator with joule-assisted heating for stable vapour generation. Appl. Therm. Eng. 230, 120770.
Tian, S., Li, X., Ren, J., Zhou, Z., Wang, F., Shi, K., Xu, J., Gu, T., Shon, H., 2024. Emerging heat-localized solar distillation systems: solar interfacial distillation vs photothermal membrane distillation. Desalination 572, 117147.
Tian, J., Mu, X., Wang, Y., Zhao, H., Yin, L., Zhang, F., Wang, X., Miao, L., 2025. Hierarchical solar interface evaporator derived from natural multilevel plant leaves for high-efficiency desalination. Chem. Eng. J. 524, 169468.
UN-Water, 2024. The united nations world Water development report 2024: water for prosperity and peace. Available at: https://www.unwater.org/publications/un-world-water-development-report-2024.
Wang, L., He, Q., Yu, H., Jin, R., Zheng, H., 2022. A floating planting system based on concentrated solar multi-stage rising film distillation process. Energy Convers. Manag. 254, 115227.
Wu, Y., Kong, R., Ma, C., Li, L., Zheng, Y., Lu, Y., Liang, L., Pang, Y., Wu, Q., Shen, Z., Chen, H., 2022. Simulation-guided design of bamboo leaf-derived carbon-based high-efficiency evaporator for solar-driven interface water evaporation. Energy Environ. Mater. 5 (4), 1323–1331.
Xia, Y., Wu, J., Shi, M., Wang, S., Zhang, Z., 2022. China's regional imbalance in electricity demand, power and water pricing: from the perspective of electricity-related virtual water transmission. Energy 257, 124775.
Xiao, C., Yin, M., Zeng, H., Hasi, Q.-M., Zhang, Y., Zhao, S., Chen, L., Li, A., 2025. Recent progress of solar-driven interfacial evaporation based on salt-resistant and oil-repellent materials. Chem. Eng. J. 508, 161009.
Yang, H., Sun, Y., Peng, M., Cai, M., Zhao, B., Li, D., Liang, Z., Jiang, L., 2022. Tailoring the salt transport flux of solar evaporators for a highly effective salt-resistant desalination with high productivity. ACS Nano 16 (2), 2511–2520.
Yang, H., Li, D., Zheng, X., Zuo, J., Zhao, B., Li, D., Zhang, J., Liang, Z., Jin, J., Ju, S., Peng, M., Sun, Y., Jiang, L., 2023. High freshwater flux solar desalination via a 3D plasmonic evaporator with an efficient heat-mass evaporation interface. Adv. Mater. 35 (47), e2304699.
Yu, J., Wang, Y., 2022. Policies on seawater desalination and water security in China: evolution, challenges and recommendations for the future. J. Clean. Prod. 336, 130415.
Yu, H., Wang, D., Jin, H., Wu, P., Wu, X., Chu, D., Lu, Y., Yang, X., Xu, H., 2023. 2D MoN1.2-rGO stacked heterostructures enabled water state modification for highly efficient interfacial solar evaporation. Adv. Funct. Mater. 33 (24), 202214828.

Yu, Z., Hu, J., Liu, G., Liu, Y., Chang, S., Rodrigue, D., Wang, X., 2024. Micronleaf-shape graphene interfaces on wood transverse sections as advanced photothermal evaporators for water purification. J. Mater. Sci. Technol. 193, 81–89.
Yuan, X., Sun, Y., Chen, W., Liu, W., Li, J., 2025. Research progress and strategy of improving evaporation performance of solar driven interface evaporation system by designing special structure. Chem. Eng. J. 503, 158705.
Zhang, L., Xu, Z., Bhatia, B., Li, B., Zhao, L., Wang, E.N., 2020a. Modeling and performance analysis of high-efficiency thermally-localized multistage solar stills. Appl. Energy 266, 114864.
Zhang, L., Zhao, L., Wang, E.N., 2020b. Stefan flow induced natural convection suppression on high-flux evaporators. Int. Commun. Heat Mass Transf. 110, 104255.
Zhang, Z., Zhang, Q., Zhang, H., Zuo, X., Yang, Q., Tang, H., Jin, S., Li, G., 2024. A 3D aerogel evaporator for efficient solar interfacial evaporation: breaking through the upper limit of steam production rate. Chem. Eng. J. 499, 156520.
Zhang, H., Miao, J., Ning, X., Fan, T., 2024. Photothermal/Magnetothermal coupled polyphenylene sulfide composite membranes for ultra-efficient and continuous seawater desalination. Desalination 592, 118163.
Zhang, C., Yan, Y., Shen, K., Xue, Z., Wu, Y., Yang, Z., Bao, Y., 2025. Synthesis of high-value porous carbon from waste plastics and structure regulation promote solar interface water evaporation. Sep. Purif. Technol. 355, 129622.
Zhang, S., Liu, M., Yang, J., Wang, J., Fang, Z., Bao, C., 2025. Capillary reinforcement strategy guided construction of robust oxygen functionalized carbon-based porous foam for highly efficient solar evaporation. Sep. Purif. Technol. 354, 129179.
Zhang, C., Yan, Y., Wu, Y., Xue, Z., Hu, Y., Li, Y., Yang, Z., 2025. Economical cobalt metal organic framework derived magnetic porous carbon achieves high flow interfacial evaporator with excellent photothermal and magnetothermal conversion capacity. Energy Convers. Manag. 342, 120140.
Zhang, C., Yan, Y., Wu, Y., Liu, C., Huang, J., Hu, Y., Li, Y., Yang, Z., 2026. Phase-change-integrated magnetic porous carbon for synergistic magnetothermal and photothermal interfacial evaporation. Energy Convers. Manag. 349, 120813.
Zhou, H., Xue, C., Chang, Q., Yang, J., Hu, S., 2021. Assembling carbon dots on vertically aligned acetate fibers as ideal salt-rejecting evaporators for solar water purification. Chem. Eng. J. 421, 129822.